Nanoscale

COMMUNICATION

View Article Online
View Journal | View Issue

Cite this: *Nanoscale*, 2016, **8**, 12531

Received 5th January 2016,
Accepted 26th January 2016

DOI: 10.1039/c6nr00060f

www.rsc.org/nanoscale

A novel photoacoustic nanoprobe of ICG@PEG-Ag_2S for atherosclerosis targeting and imaging *in vivo*†

Chenxin Wu,[a] Yejun Zhang,[a] Zhen Li,[b] Chunyan Li*[a] and Qiangbin Wang*[a]

Atherosclerosis is a major cause of cardiovascular and cerebrovascular diseases that have high mortality and disability rates. Because of its unclear pathogenic mechanism and heterogeneous distribution feature, it is still a big challenge to achieve precise diagnosis and therapy of atherosclerosis at its early stage *in vivo*. Herein, we fabricated a new ICG@PEG-Ag_2S nanoprobe by a simple self-assembly of DT-Ag_2S QDs, amphipathic C18/PEG polymer molecules and ICG. The ICG@PEG-Ag_2S nanoprobe showed relatively long blood retention and was selectively accumulated in the region of atherosclerotic plaque due to the lipophilicity of the C18 chain to the atherosclerosis microenvironment, and thus the atherosclerosis was real-time monitored by high contrast-enhanced photoacoustic (PA) imaging of ICG. Combining the high signal-to-noise ratio (SNR) and high spatial resolution fluorescence imaging of Ag_2S QDs in the second near-infrared window (NIR-II) and related histological assessment *in vitro*, the feasibility of this new nanoprobe for atherosclerosis targeting in an Apoe$^{-/-}$ mouse model was verified. Additionally, hemolysis and coagulation assays of the ICG@PEG-Ag_2S revealed its decent hemocompatibility and no histological changes were observed in the main organs of the mouse. Such a simple, multifunctional nanoprobe for targeting and PA imaging of atherosclerosis will have a great potential for future clinical applications.

Introduction

Atherosclerosis, an inflammatory disease of the arterial system, has become a leading cause of cardiac infarction, brain stroke and other serious complications.[1] Since the formation of atherosclerosis is a very slow process, it is very difficult to identify it at its early stage. Thus, development of new imaging techniques that can provide anatomic and hemodynamic information with high spatial and temporal resolution would be of great help for atherosclerosis diagnosis and therapy. So far, various noninvasive imaging techniques have been explored to assess vascular wall and plaque compositions.[2–9] However, magnetic resonance imaging (MRI) suffers from a poor signal strength, resulting in a low sensitivity, and computed tomography (CT) is limited by poor soft tissue contrast. More importantly, both CT and MR imaging need long acquiring and post-processing times, which could not provide the real-time anatomic and functional information on lesion regions. In addition, some other imaging approaches such as single photon emission computed tomography (SPECT) and positron emission tomography (PET) have also been employed for atherosclerosis assessment but limited by their spatial resolution.

Photoacoustic (PA) imaging is an emerging technology which combines the inherent advantages of ultrasound and optical imaging, possessing high sensitivity, high tissue penetration depth, and three-dimensional (3D) quantitative function,[10,11] and shows a great potential for atherosclerosis diagnosis and assessment. However, there have been few reports on PA imaging of atherosclerosis due to the lack of available PA imaging agents which can efficiently target the atherosclerosis.[12,13] Indocyanine green (ICG), a near-infrared (NIR) dye in clinical practice, has been explored as a PA agent for biomedical applications due to its unique absorption and emission properties in the NIR region.[14–16] However, free ICG is greatly limited by its aggregation in aqueous solutions, nonspecific binding to proteins, and rapid liver elimination from the body.[17,18]

In this study, we fabricated a complex ICG@PEG-Ag_2S nanoprobe as a PA agent for *in vivo* atherosclerosis diagnosis and imaging by a simple mixing of DT-Ag_2S QDs, amphipathic C18/PEG polymer molecules and ICG. This ICG@PEG-Ag_2S nanoprobe exhibited relatively long blood retention and was selectively accumulated in the region of atherosclerotic plaque

[a]*Key Laboratory of Nano-Bio Interface, Division of Nanobiomedicine and i-Lab, CAS Center for Excellence in Brain Science, Suzhou Institute of Nano-Tech and Nano-Bionics, Chinese Academy of Sciences, Suzhou 215123, China. E-mail: qbwang2008@sinano.ac.cn, cyli2012@sinano.ac.cn; Fax: (+)86-512-62872620*

[b]*School of Radiation Medicine and Protection, Soochow University, Suzhou 215123, China*

†Electronic supplementary information (ESI) available. See DOI: 10.1039/c6nr00060f

due to the lipophilicity of the C18 chain to the atherosclerosis microenvironment, providing high contrast-enhanced PA imaging of atherosclerotic plaque *in vivo*. These observations were further confirmed by high signal-to-noise ratio (SNR) and high spatial resolution fluorescence imaging of Ag_2S QDs in the second NIR window (NIR-II) and histological analysis, suggesting the capability of the ICG@PEG-Ag_2S nanoprobe for atherosclerosis targeting and imaging.

Results and discussion

Design, synthesis and properties of ICG@PEG-Ag_2S

A complex ICG@PEG-Ag_2S nanoprobe was prepared by a simple self-assembly process,[19,20] in which the optimized formulation is 24 nM of ICG in 1 mg mL^{-1} Ag_2S (Fig. S1,† see the Experimental section for details). The transmission electronic microscopy (TEM) image illustrated the good dispersity of DT-Ag_2S, PEG-Ag_2S and ICG@PEG-Ag_2S with a core diameter of ~3.3 nm (Fig. 1A, B and S2†). The hydrodynamic sizes of PEG-Ag_2S and ICG@PEG-Ag_2S obtained by dynamic light scattering (DLS) were about 166.3 nm and 172.2 nm, respectively, which were much larger than for DT-Ag_2S (3.4 nm) dispersed in chloroform (Fig. 1C). The optical properties of ICG, PEG-Ag_2S and ICG@PEG-Ag_2S were characterized as shown in Fig. 1D and S3.† In comparison with PEG-Ag_2S, ICG@PEG-Ag_2S presented an obvious absorption peak at ~800 nm and the emission peak at 1100 nm has a slight attenuation in fluorescence intensity.

In order to assess the tissue penetration of the as-prepared PA probe, phantom images of agarose in a cone-shaped tube containing ICG@PEG-Ag_2S and free ICG were scanned with a photoacoustic instrument at different depths. As shown in Fig. 2 and S4,† *in vitro* PA imaging studies showed that both free ICG and ICG@PEG-Ag_2S could be detected at more than 9.9 mm, indicating their high tissue penetration depth. It also revealed a high detection sensitivity down to 0.192 nM after the injection of these two materials, respectively, at a depth of ~2 mm underneath the skin of a living mouse, but free ICG showed some dispersion phenomena in comparison with ICG@PEG-Ag_2S. Furthermore, the PA signal had a good linear relationship with the ICG@PEG-Ag_2S concentrations, which promises a quantitative analysis of the *in vivo* imaging based on the PA signal (Fig. 2B).

To target the atherosclerosis plaque, a long blood circulation time of the ICG@PEG-Ag_2S nanoprobe becomes notably important. The blood circulation time of ICG@PEG-Ag_2S in the Kunming mice was analyzed by intravenously injecting 10 mg kg^{-1} of ICG@PEG-Ag_2S. 20 μL of blood was collected from the caudal vein at different time points and the fluorescence intensity of the blood was quantitated using a NIR-II fluorescence instrument. As shown in Fig. S5 and S6,†

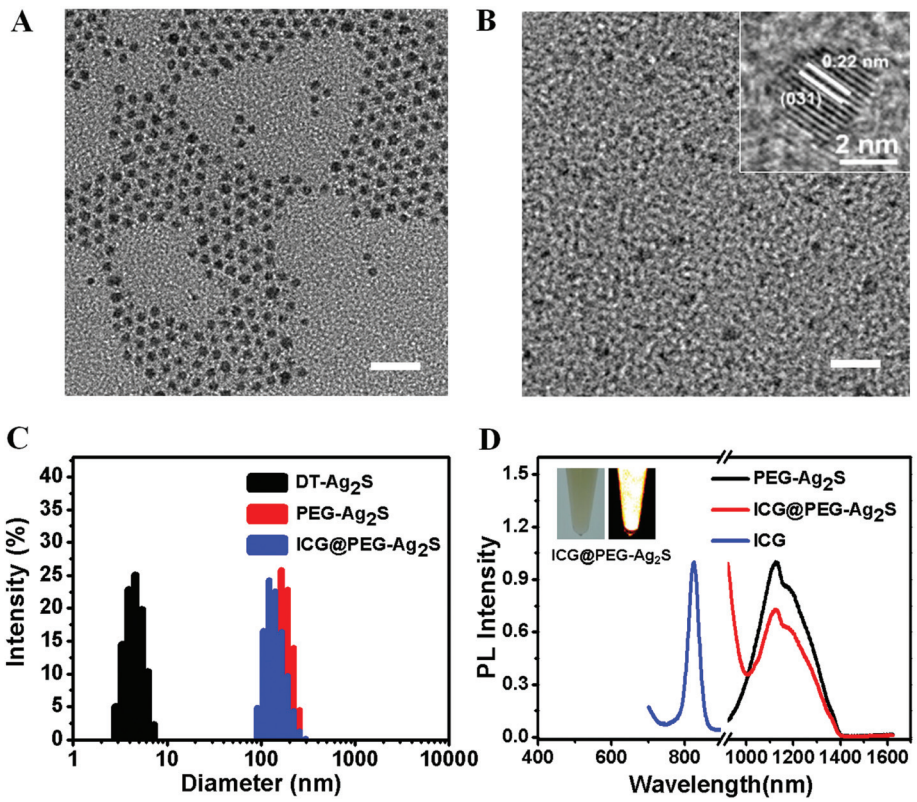

Fig. 1 Characterization of the ICG@PEG-Ag_2S nanoprobe. (A) TEM image of DT-Ag_2S. (B) TEM image of ICG@PEG-Ag_2S. (C) DLS data of DT-Ag_2S, PEG-Ag_2S and ICG@PEG-Ag_2S. (D) Fluorescence emission spectra of ICG, PEG-Ag_2S and ICG@PEG-Ag_2S.

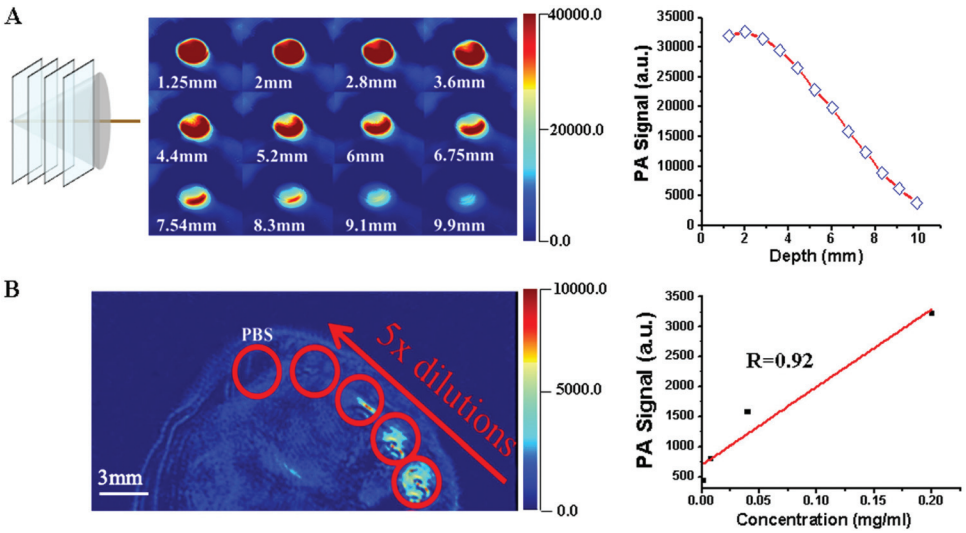

Fig. 2 Tissue penetration depth and imaging sensitivity of the ICG@PEG-Ag_2S nanoprobe. (A) Phantom images of a cone-shaped agarose tube containing ICG@PEG-Ag_2S (24 nM ICG in 1 mg mL^{-1} Ag_2S) at different depths. (B) The PA signal sensitivity of ICG@PEG-Ag_2S at a depth of 2 mm underneath the skin of a living mouse after the injection of the nanoprobe at various concentrations from 0.008 to 0.2 mg per mL of Ag_2S (24 nM ICG in 1 mg mL^{-1} Ag_2S).

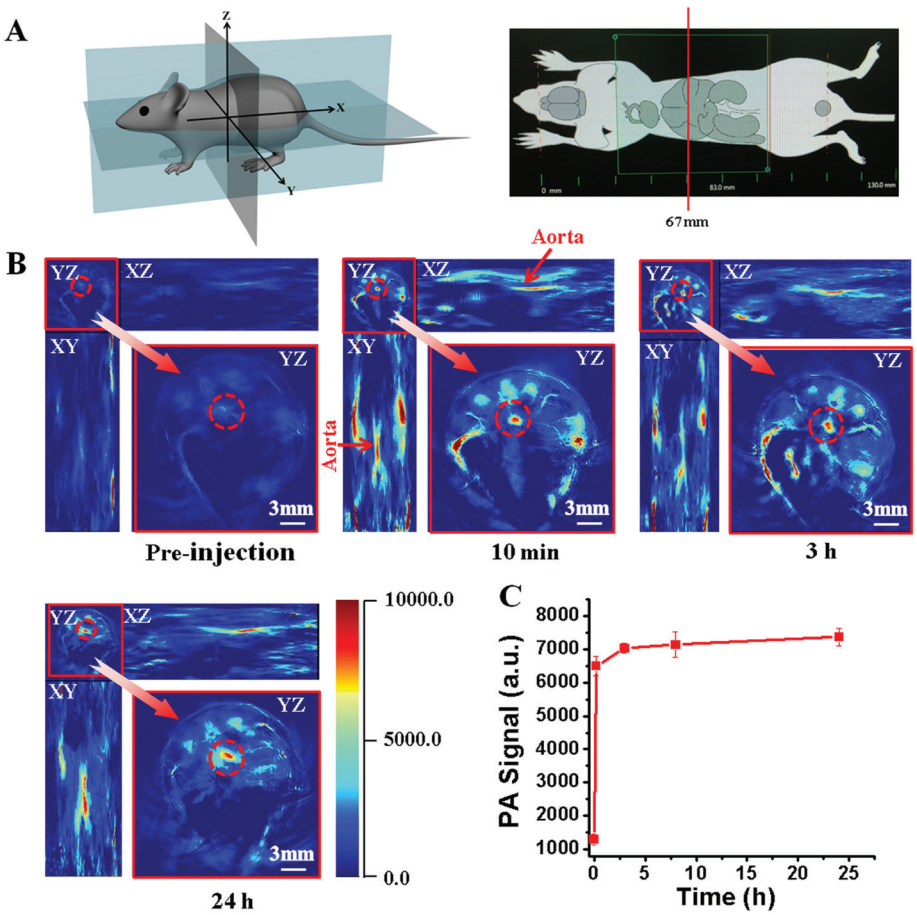

Fig. 3 (A) Graphical views of the PA imaging of living mice. (B) Time course of PA imaging of $Apoe^{-/-}$ mice after intravenous injection of ICG@PEG-Ag_2S. The transverse view (YZ) of the mouse was acquired at 67 mm starting from the origin. (C) Quantitative analysis of PA signals in the aorta of the mouse corresponding to the red circle in B over time.

ICG@PEG-Ag_2S exhibited a long half-life time of 6.88 h, which was much higher than that of free ICG (1.97 min), providing the nanoprobe more opportunity to target the atherosclerosis plaques.

In vivo real-time visualization of atherosclerosis with PA imaging

Previous studies have shown that atherosclerosis was caused by lipid accumulation, which resulted in chronic inflammation responses and further induced extensive phagocytic cells, especially macrophages, and was recruited in the lesion region.[1,21] The deep tissue penetration and high SNR of the PA signal, as well as the appropriate blood retention time of ICG@PEG-Ag_2S nanovesicles, endow it with great potential for noninvasive diagnosis of atherosclerosis *in vivo*. To assess the feasibility of ICG@PEG-Ag_2S for atherosclerosis plaque detection in living mice, $ApoE^{-/-}$ mice were intravenously injected ICG@PEG-Ag_2S (10 mg kg^{-1}), and PA imaging was performed pre- and post-injection at 10 min, 1, 3, 8 and 24 h, respectively, using a photoacoustic tomography system (inVision 256, iThera Medical). Fig. 3A shows graphical views of the PA imaging of living mice. As shown in Fig. 3B, it showed an image with negligible contrast in the whole body of the mouse, while after the injection of ICG@PEG-Ag_2S, a remarkable enhancement of the PA intensity in the region of the aorta was observed over time. In contrast, we observed a very weak PA signal intensity in the mouse after administration of the same amount of free ICG (Fig. S7†), then a slight enhancement of the PA intensity was observed in the aorta, but it soon disappeared at 1 h post-injection, which could be attributed to its short blood circulation time. Quantitative analysis of the PA intensity at 3 h post-injection of ICG@PEG-Ag_2S indicated a nearly 6-fold enhancement compared with that of pre-injection and then sustained over 24 h (Fig. 3C), which provided an ideal time-window for atherosclerosis plaque detection.

Detection of atherosclerosis in the aortas with NIR-II fluorescence imaging, and correlation with histological assessment

To further verify the PA imaging results, the mice were sacrificed and the aortas were harvested from the $ApoE^{-/-}$ and C57BL/6 mice after intravenous injection of ICG@PEG-Ag_2S. Due to the intrinsic advantages of NIR-II fluorescence imaging,[22–28] Ag_2S QD enabled the *in vitro* imaging of tiny atherosclerotic plaques with high spatial resolution and high contrast. As shown in Fig. 4 and S8,† it was evident that the NIR-II fluorescence signals of the aorta from the $ApoE^{-/-}$ mice were much stronger than those of C57BL/6 mice with brighter fluorescence spots along the aorta, which indicated the atherosclerotic plaques. The specific labeling of atherosclerotic plaques by Ag_2S QDs was ascribed to the lipophilicity of the C18 chain on the Ag_2S QD surface to the atherosclerosis microenvironment. This observation was supported by the Oil Red O staining of the aorta, which was a typical pigment used for lipid staining. To further identify the atherosclerotic plaques, the sections of aortas were stained with Sudan III. As shown in

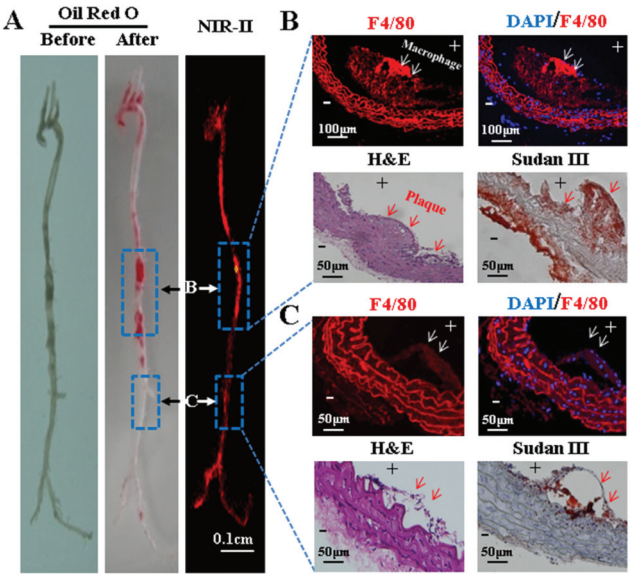

Fig. 4 *Ex vivo* imaging of atherosclerotic plaques and correlation with histological assessment. (A) Brightfield and NIR-II fluorescence imaging of the aortas. The aortas were harvested from the $ApoE^{-/-}$ mice after intravenous injection of ICG@PEG-Ag_2S and further stained with Oil Red O. (B, C) H&E and immunohistochemical staining of the dissected aortas corresponding to panel A. White arrows indicate macrophages and red arrows indicate atherosclerotic plaques.

Fig. 4B, dark red stains indicated the typical atherosclerotic plaques corresponding to the brightfield and NIR fluorescence images. Thanks to the high sensitivity of fluorescence imaging with NIR-II Ag_2S QDs, tiny atherosclerotic plaques could also be detected unambiguously (Fig. 4C). Furthermore, the slices of aortas were stained with a mouse F4/80 antibody; they showed a macrophage-rich region in the margin of atherosclerotic plaques, which were consistent with a previous report.[1]

Excellent hemocompatibility and negligible toxicity

On the basis of all the above results, the ICG@PEG-Ag_2S nanoprobe showed a commendable capability for targeting and imaging of atherosclerosis. Considering its potential clinical practice, the biocompatibility and toxicity of ICG@PEG-Ag_2S were then investigated carefully. First, the hemocompatibility of ICG@PEG-Ag_2S was assessed by incubating the nanoprobe with human red blood cells (RBCs) for 2 h. As shown in Fig. 5A, it showed that the hemolysis percentage was 1.05% even at a high concentration of Ag_2S (1000 μg mL^{-1}), indicating its decent hemocompatibility. In addition, activated partial thromboplastin time (APTT) and prothrombin time (PT) were used to evaluate coagulation abnormalities in the intrinsic pathway and extrinsic pathway. The results demonstrated that there was no obvious difference between the experimental and control groups (Fig. 5B and C), suggesting the negligible effect of ICG@PEG-Ag_2S on coagulation. For a further assessment of the biocompatibility of ICG@PEG-Ag_2S *in vivo*, Kunming mice treated with different

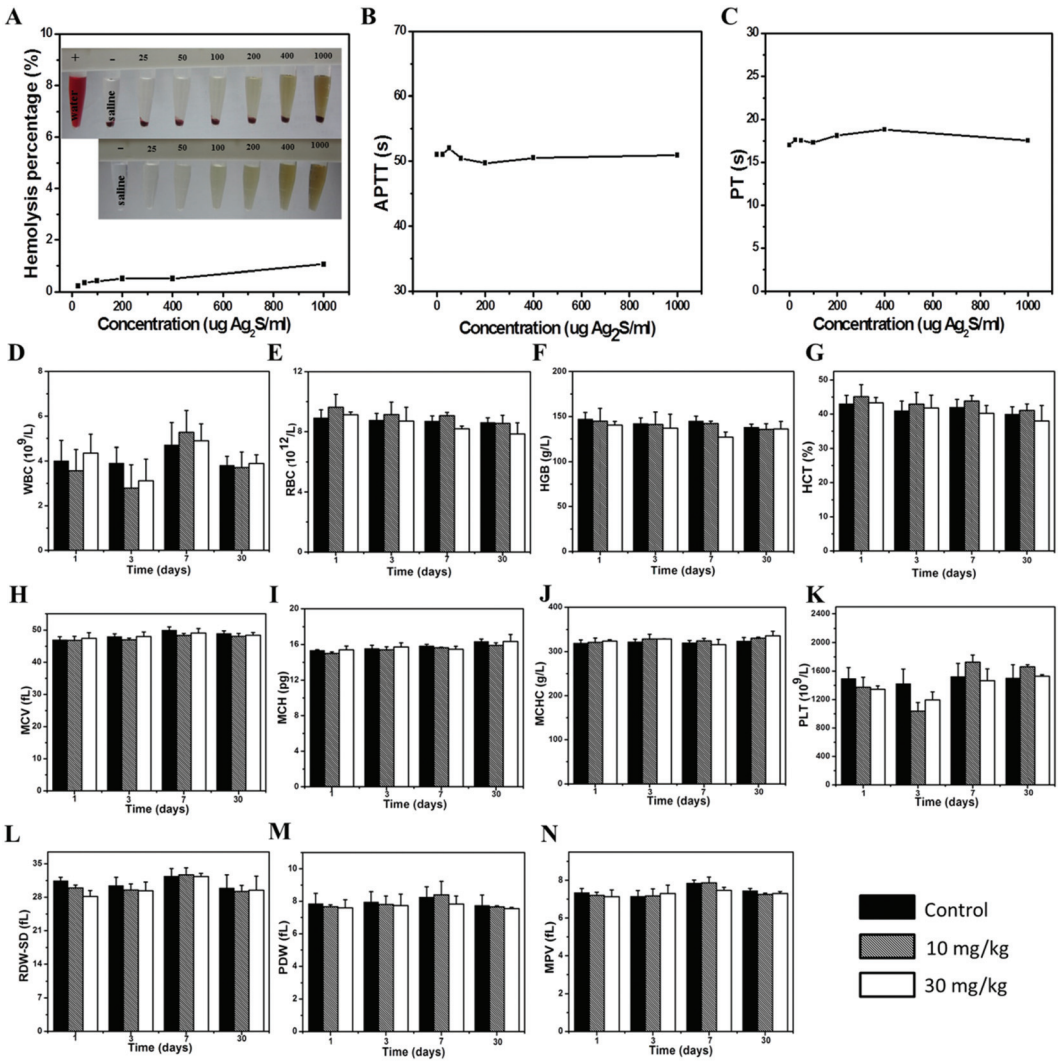

Fig. 5 Hemocompatibility assay of the ICG@PEG-Ag_2S probe. (A–C) Hemolysis and blood coagulation results of ICG@PEG-Ag_2S with various concentrations (25, 50, 100, 200, 400 and 1000 μg Ag_2S per mL). (D–N) Hematology data of Kunming mice treated with ICG@PEG-Ag_2S (10 and 30 mg kg^{-1}) at days 1, 3, 7, 30, respectively.

dosages of ICG@PEG-Ag_2S (10 and 30 mg kg^{-1}, n = 3) were sacrificed at days 1, 3, 7 and 30, respectively. After collecting 500 μL of blood samples from the mice' fundus arteries, the white blood cells, red blood cells, and hemoglobin were analyzed. It was found that there was no significant difference in comparison with the control group, representing the high hemocompatibility of the ICG@PEG-Ag_2S nanoprobe. Although the number of platelets and white blood cells presented a slight drop at the beginning, they went back to normal levels after a few days (Fig. 5D–N), which might be attributed to the acute immune response by ICG@PEG-Ag_2S.

In addition, the main organs of mice including the heart, liver, spleen, lung and kidney were harvested and stained with hematoxylin/eosin at days 1, 3, 7 and 30 after the injection of ICG@PEG-Ag_2S at a dose of 30 mg kg^{-1}, respectively. As shown in Fig. 6, negligible toxicity of ICG@PEG-Ag_2S was observed, indicating its decent biocompatibility *in vivo*.

Conclusions

In summary, we successfully developed an ICG@PEGAg_2S nanoprobe as a simple but effective PA agent for highly sensitive detection of atherosclerosis in a living mouse model, in which ICG offers high contrast PA signals and C18/PEG capped Ag_2S works as the carrier to provide ICG a decent blood circulation half-time and good lipophilicity to the atherosclerosis microenvironment. By taking advantage of the long blood circulation and lipophilicity of the ICG@PEG-Ag_2S nanoprobe, atherosclerotic plaques were imaged in a high contrast-enhanced and real-time manner after intravenous injection of ICG@PEG-Ag_2S even without conjugation with any targeting ligand. The integral plaques in the aorta were clearly revealed by ICG PA imaging, and were further confirmed by Ag_2S QD fluorescence imaging and classical histological assessment. Hemolysis and coagulation assays of the

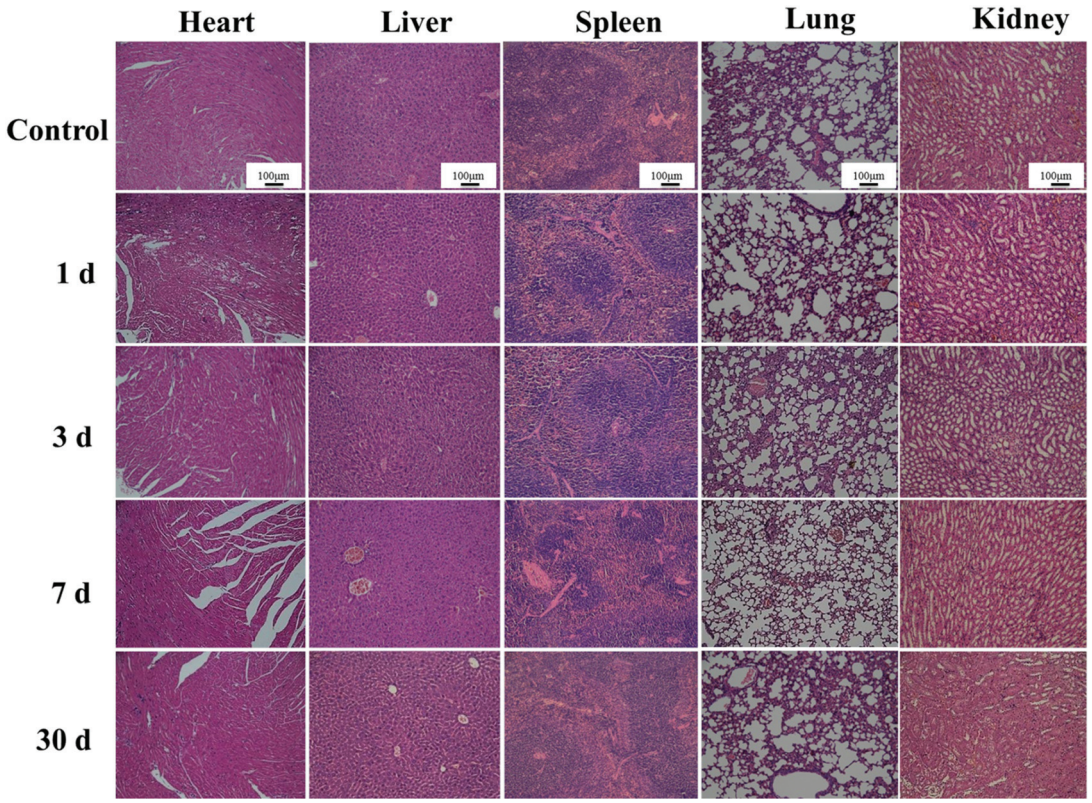

Fig. 6 Tissue toxicity assay of the ICG@PEG-Ag_2S nanoprobe. H&E staining of major tissues from nude mice after injection of PBS (control) or ICG@PEG-Ag_2S (30 mg kg^{-1}) at different time points.

ICG@PEG-Ag_2S revealed its decent hemocompatibility. No histological change was observed in the main organs of the mouse after administration of ICG@PEG-Ag_2S for 1 month, indicating negligible toxicity of this nanoprobe. We expect that our results presented here will further prompt the development of novel strategies for targeting, imaging and treatment of atherosclerosis in the clinic.

Experimental section

Materials

1-Dodecanethiol (DT, 98%), chloroform, ethanol, Sudan III, Hematoxylin–Eosin (HE), regular agarose and dimethyl sulfoxide (DMSO) were all obtained from Sinopharm Chemical Reagent Company. Oil Red O, *N*-(3-dimethylaminopropyl)-*N*-ethylcarbodiimide hydrochloride (EDC), isopropanol and intralipid were purchased from Sigma Aldrich. Indocyanine green (ICG) was purchased from Panreac AppliChem. An Amicon Ultra-15 Centrifugal Filter Unit was obtained from Millipore. Matrigel™ was purchased from Corning/Becton Dickinson. BSA (Biotime), a Mouse F4/80 Antibody (R&D Systems) and a Goat Anti-Rat IgG (Abcam) were used for immunofluorescence staining. A HemosIL™ kit was purchased from Instrumentation Laboratory Company (MA 02421-3125). Deionized water was obtained from a Milli-Q ion-exchange system.

Synthesis of C18PMH/PEG-Ag_2S QDs

Polyethylene glycol-grafted amphiphilic poly-methoxy poly (C18/PEG) was synthesized according to a previously reported method.[29] Briefly, 80 mg C18/PEG was added to 4 mg DT-Ag_2S dissolved in chloroform. After 1 h sonication, the chloroform was removed *via* rotary evaporation. The remainder was then dissolved in phosphate buffered saline (PBS, pH = 7.4). The product was washed three times with PBS through ultrafiltration using an Amicon with a 100 kDa MW cut-off and isolated by centrifugation at 10 000 rpm for 2 min, and then dispersed in PBS for further use.

Loading of ICG in C18PMH/PEG-Ag_2S QDs

To achieve the best imaging effect of ICG@PEG-Ag_2S in both photoacoustic (PA) and NIR-II fluorescence imaging modalities, the ICG@PEG-Ag_2S containing 1 mg PEG-Ag_2S was mixed with different concentrations of ICG (in DMSO) at 0, 16, 32, 64, 128 and 256 nM, respectively. After stirring for 15 h and removing the free ICG, the ICG@PEG-Ag_2S was added to a 96-well ELISA plate with increasing concentrations. The plate was exposed to the photoacoustic instruments. After fitting of hyperbolic curves, the optimal dose of ICG was 24 nM (0.02 mg mL^{-1}) in 1 mg PEG-Ag_2S (denoted as 1 mg mL^{-1} ICG@PEG-Ag_2S). After ICG (0.2 mg) dissolved in 2 mL DMSO, the solution was mixed with 20 mL PEG-Ag_2S (1 mg mL^{-1}) in PBS, and then stirred for 15 h away from light at room tem-

perature. Free ICG was discarded through ultrafiltration three times.

Characterization

A Tecnai G2 F20S twin transmission electron microscope (TEM, FEI, USA) was used to detect the surface morphology of DT-Ag_2S, PEG-Ag_2S and ICG@PEG-Ag_2S, which was operated at 200 kV. A Zetasizer Nano ZS (Malvern) was used to measure the hydrodynamic sizes of the DT-Ag_2S, PEG-Ag_2S and ICG@PEG-Ag_2S. A Perkin-Elmer Lambda 25 UV-vis spectrometer was used to collect the UV-vis-NIR absorption spectra at room temperature. The range was 350–900 nm. We recorded the NIR-II fluorescence spectra on an Applied NanoFluorescence spectrometer with an excitation laser source of 785 nm at room temperature.

In vitro and *in vivo* detection of ICG@PEG-Ag_2S

***In vitro* depth of penetration.** To understand the penetration depth acquired by photoacoustic imaging, we constructed a cone shaped plastic container tissue-mimicking phantom, which was based on 3% agarose and 1% intralipid to mimic tissue scattering. ICG@PEG-Ag_2S (24 nM ICG) mixed in liquid agarose solution was embedded in a 3 mm diameter pipette tip. After the inclusions solidified, the pipette tip was inserted into the plastic container. After the agarose in the container solidified, we measured the cone sections using a multispectral optoacoustic tomography system (iThera Medical).

***In vivo* sensitivity.** To measure the detection sensitivity of the ICG@PEG-Ag_2S *in vivo*, ICG@PEG-Ag_2S solutions at different concentrations (0.008, 0.04, 0.2 mg mL^{-1} Ag_2S) were mixed with Matrigel at a 1 : 1 ratio. When the solutions were semi-set, they were injected subcutaneously (100 μL) into the lower back of nude mice (n = 3). After the solidification of the Matrigel, the back of the mouse was scanned with the photoacoustic instrument. Free ICG (0.192, 0.96, 4.8, 24 nM) was also measured as the control group.

Blood circulation. To understand the best target time for the atherosclerosis plaque, we measured the ICG@PEG-Ag_2S retained in blood circulation, and free ICG was the control group. After intravenously injecting ICG@PEG-Ag_2S (10 mg kg^{-1}) or free ICG (24 nM) into the Kunming mice (10 mg kg^{-1}), 20 μL of blood anticoagulated with heparin sodium was obtained from the caudal vein at different time points (5, 30 min, 1, 10, 24, 48 h) and placed in a standard 96-well plate orderly, and then quantified using the NIR-II fluorescence instrument.

Toxicity study

Hemolysis assays. Fresh human blood anti-coagulated with Ethylenediamine Tetraacetic Acid Dipotassium salt dehydrate (EDTA-2K) was drawn from a healthy volunteer, which was approved by the legally appropriate Ethical Committee. After centrifuging fresh human blood at 3000 rpm for 10 min, the upper solution was sucked out and the red blood cells (RBCs) were rinsed by sodium chloride injection 5 times. The collected RBCs were diluted with sodium chloride injection (1 : 9, v/v). The ICG@PEG-Ag_2S was diluted by sodium chloride injection with concentrations in the range from 25 μg mL^{-1} to 1000 μg mL^{-1} (25, 50, 100, 200, 400 and 1000 μg mL^{-1}). 0.3 mL of 10% RBC solutions were mixed with 1.2 mL sample solution and incubated for 2 h at room temperature, as the sodium chloride injection was a negative control and the deionized water was a positive control. After centrifuging the solutions at 4000 rpm for 3 min, the absorbance of the upper solution was measured on a Perkin-Elmer Lambda 25 UV-vis spectrometer at a wavelength of 541 nm. The hemolysis rate was calculated as the difference between the sample absorbance and the negative control absorbance divided by the difference between the positive and negative control absorbances.

Coagulation assay. The plasma was obtained from the upper solution of the centrifuged fresh human blood. 50 μL of sodium chloride injection was mixed with various concentrations of the ICG@PEG-Ag_2S and then incubated with 500 μL plasma for 5 min. After being centrifuged at 4000 rpm for 2 min, the upper solutions were sucked out to measure activated partial thromboplastin time (APTT) and prothrombin time (PT) on a Chrono-Log 560-Ca Platelet Aggregation Analyzer using a HemosIL™ kit.

Hematology and pathology analysis. 500 μL of blood samples anti-coagulated with EDTA-2K were obtained from the fundus arteries of Kunming mice at days 1, 3, 7 and 30 after intravenously injecting 200 μL of ICG@PEG-Ag_2S (10 and 30 mg kg^{-1}), and PBS was the control group. The blood hematology analysis was completed at Shanghai Research Center for Model Organisms. After the mice were killed, they were injected with 30 mg kg^{-1} ICG@PEG-Ag_2S, and different tissues (heart, liver, spleen, lung and kidneys) were extracted at days 1, 3, 7 and 30, respectively. The organs were fixed in 10% formaldehyde and embedded in paraffin. The tissues were stained with hematoxylin–eosin and analyzed using a Nikon Eclipse 80i microscope (Nikon) after being sectioned at 5 μm thickness.

Animal protocol

8-Week-old male Apolipoprotein (Apo) $E^{-/-}$ mice, 6-week-old female Kunming mice and 10-week-old female nude mice were obtained from Department of Laboratory Animal Science, Peking University Health Science Center, China. The experiments were carried out with the Guidelines for the Care and Use of Research Animals. Apo$E^{-/-}$ mice were fed on a western diet (containing 21% fat and 0.15% cholesterol) for >25 weeks and used for PA and NIR-II fluorescence imaging. To confirm that the atherosclerosis model was successfully established, the mouse body weights were measured weekly for 25 weeks and photos were taken to observe the changes in mice appearance. The mice were anesthetized with isoflurane and intravenously injected with 200 μL ICG@PEG-Ag_2S or 200 μL free ICG (control group). PA imaging was performed at pre- and different time points after the injection of ICG@PEG-Ag_2S or free ICG. Then NIR-II fluorescence imaging was performed followed by aortic exposure *in vivo*. Aortas (n = 3) were transferred

to the NIR-II fluorescence imaging instrument, and stained with Sudan III (frozen sectioning), hematoxylin–eosin and immunofluorescence (paraffin section) to identify atherosclerotic lesions. Kunming mice were prepared for the ICG@PEG-Ag_2S *in vivo* toxicity experiments. The mice were intravenously injected with 200 μL ICG@PEG-Ag_2S at a dosage of 10 and 30 mg kg^{-1}, and 200 μL PBS was the control group, respectively. After the mice were sacrificed, their blood and organs were extracted at days 1, 3, 7 and 30 post-injection.

Photoacoustic imaging of mice

The photoacoustic imaging (PA) studies of mice were performed on a preclinical photoacoustic computerized tomography scanner (inVision 256, iThera Medical). The following parameters of the system were adopted: illumination wavelength (780 nm corresponding to the absorption peak of ICG), pulse energy (80–100 mJ), laser fluence (200 mW cm^{-2}), central frequency (~5 MHz), and bandwidth (>50%). The $ApoE^{-/-}$ mice (n = 3) were anesthetized using 3% isoflurane with oxygen delivered *via* a nose cone during injection and imaging. The PA images were acquired at pre- and different time points (10 min, 1, 3, 8 and 24 h) after intravenous injection of 200 μL ICG@PEG-Ag_2S (10 mg kg^{-1}) or 200 μL free ICG (24 nM). The PA signals of the aorta were collected using multispectral optoacoustic tomography software.

NIR-II fluorescence imaging of mice

NIR-II fluorescence imaging was performed with the $ApoE^{-/-}$ mice aorta (n = 3) exposure *in vitro* at 24 h after the injection of ICG@PEG-Ag_2S with C57BL/6 mice as the control group. After fixing in 10% formaldehyde for 30 min, the aortas were stained with 0.5% Oil Red O in isopropanol for 1 h, and free Oil Red O was decolored using 75% ethyl alcohol, then the remaining red region indicated atherosclerosis.

Histology assay

To further identify the atherosclerotic plaques, sections of aortas were stained with Sudan III, hematoxylin–eosin (H&E) and immunofluorescence to identify atherosclerotic plaques. After fixing in 10% formaldehyde for 24 h, small regions of the aortas were frozen in chilled isopentane and sectioned at 5 μm thickness. The Sudan III staining was performed for lipid upon macrophages, and the H&E staining for the entire plaque morphology. Images were taken using a Nikon Ti microscope. The macrophages were detected and calculated by immunofluorescence staining with a mouse F4/80 antibody. After washing with PBS, a fluorescent Alexa Fluor dye conjugated goat anti-rat IgG (1 : 200) secondary antibody was applied.

Acknowledgements

This work was financially supported by the Chinese Academy of Sciences "Strategic Priority Research Program" (No. XDA01030200), the National Natural Science Foundation of China (No. 21303249, 21425103, and 81401464), and the Natural Science Foundation of Jiangsu Province (BK20130366).

References

1 P. Libby, *Circulation*, 2002, **105**, 1135–1143.
2 Z. Zhang, J. Machac, G. Helft, S. Worthley, C. Tang, A. Zaman, O. Rodriguez, M. Buchsbaum, V. Fuster and J. Badimon, *BMC Nucl. Med.*, 2006, **6**, 3.
3 J. Sanz and Z. A. Fayad, *Nature*, 2008, **451**, 953–957.
4 M. Wildgruber, F. K. Swirski and A. Zernecke, *Theranostics*, 2013, **3**, 865–884.
5 H. Xing, S. Zhang, W. Bu, X. Zheng, L. Wang, Q. Xiao, D. Ni, J. Zhang, L. Zhou, W. Peng, K. Zhao, Y. Hua and J. Shi, *Adv. Mater.*, 2014, **26**, 3867–3872.
6 E. J. Chung, L. B. Mlinar, K. Nord, M. J. Sugimoto, E. Wonder, F. J. Alenghat, Y. Fang and M. Tirrell, *Adv. Healthcare Mater.*, 2015, **4**, 367–376.
7 C. Vinegoni, I. Botnaru, E. Aikawa, M. A. Calfon, Y. Iwamoto, E. J. Folco, V. Ntziachristos, R. Weissleder, P. Libby and F. A. Jaffer, *Sci. Transl. Med.*, 2011, **3**, 84ra45.
8 C. Parolini, M. Busnelli, G. S. Ganzetti, F. Dellera, S. Manzini, E. Scanziani, J. L. Johnson, C. R. Sirtori and G. Chiesa, *Mol. Imaging*, 2014, **13**, 1–9.
9 J. S. Yoo, J. Lee, J. H. Jung, B. S. Moon, S. Kim, B. C. Lee and S. E. Kim, *Sci. Rep.*, 2015, **5**, 11752.
10 L. V. Wang and S. Hu, *Science*, 2012, **335**, 1458–1462.
11 D. Razansky, A. Buehler and V. Ntziachristos, *Nat. Protoc.*, 2011, **6**, 1121–1129.
12 H. Qin, T. Zhou, S. H. Yang, Q. Chen and D. Xing, *Nanomedicine*, 2013, **8**, 1611–1624.
13 W. W. Li and X. Y. Chen, *Nanomedicine*, 2015, **10**, 299–320.
14 M. B. Zheng, P. F. Zhao, Z. Y. Luo, P. Gong, C. F. Zheng, P. F. Zhang, C. X. Yue, D. Y. Gao, Y. F. Ma and L. T. Cai, *ACS Appl. Mater. Interfaces*, 2014, **6**, 6709–6716.
15 C. F. Zheng, M. B. Zheng, P. Gong, D. X. Jia, P. F. Zhang, B. H. Shi, Z. H. Sheng, Y. F. Ma and L. T. Cai, *Biomaterials*, 2012, **33**, 5603–5609.
16 Q. Chen, C. Liang, C. Wang and Z. Liu, *Adv. Mater.*, 2015, **27**, 903–910.
17 A. W. Hemming, C. H. Scudamore, C. R. Shackleton, M. Pudek and S. R. Erb, *Am. J. Surg.*, 1992, **163**, 515–518.
18 A. K. Kirchherr, A. Briel and K. Mader, *Mol. Pharm.*, 2009, **6**, 480–491.
19 B. H. Dong, C. Y. Li, G. C. Chen, Y. J. Zhang, Y. Zhang, M. J. Deng and Q. Wang, *Chem. Mater.*, 2013, **25**, 2503–2509.
20 F. Hu, C. Y. Li, Y. J. Zhang, M. Wang, D. M. Wu and Q. Wang, *Nano Res.*, 2015, **8**, 1637–1647.
21 M. E. Lobatto, C. Calcagno, A. Millon, M. L. Senders, F. Fay, P. M. Robson, S. Ramachandran, T. Binderup, M. P. M. Paridaans, S. Sensarn, S. Rogalla, R. E. Gordon, L. Cardoso, G. Storm, J. M. Metselaar, C. H. Contag, E. S. G. Stroes, Z. A. Fayad and W. J. M. Mulder, *ACS Nano*, 2015, **9**, 1837–1847.

22 A. M. Smith, M. C. Mancini and S. M. Nie, *Nat. Nanotechnol.*, 2009, **4**, 710–711.
23 G. S. Hong, J. C. Lee, J. T. Robinson, U. Raaz, L. M. Xie, N. F. Huang, J. P. Cooke and H. J. Dai, *Nat. Med.*, 2012, **18**, 1841–1846.
24 G. S. Hong, S. Diao, J. L. Chang, A. L. Antaris, C. X. Chen, B. Zhang, S. Zhao, D. N. Atochin, P. L. Huang, K. I. Andreasson, C. J. Kuo and H. J. Dai, *Nat. Photonics*, 2014, **8**, 723–730.
25 G. Hong, J. T. Robinson, Y. Zhang, S. Diao, A. L. Antaris, Q. Wang and H. Dai, *Angew. Chem., Int. Ed.*, 2012, **51**, 9818–9821.
26 C. Y. Li, Y. J. Zhang, M. Wang, Y. Zhang, G. C. Chen, L. Li, D. M. Wu and Q. Wang, *Biomaterials*, 2014, **35**, 393–400.
27 C. Y. Li, L. M. Cao, Y. J. Zhang, P. W. Yi, M. Wang, B. Tan, Z. W. Deng, D. M. Wu and Q. Wang, *Small*, 2015, **11**, 4517–4525.
28 C. Li, F. Li, Y. Zhang, W. Zhang, X.-E. Zhang and Q. Wang, *ACS Nano*, 2015, **9**, 12255–12263.
29 G. Prencipe, S. M. Tabakman, K. Welsher, Z. Liu, A. P. Goodwin, L. Zhang, J. Henry and H. J. Dai, *J. Am. Chem. Soc.*, 2009, **131**, 4783–4787.